



Electrochemical Behavior of Lithium in Alkaline Aqueous Electrolytes

III. Impedance Model

Oswaldo Pensado,^{a,*} Mirna Urquidi-Macdonald,^{b,**} and Digby D. Macdonald^{c,**}

^aCenter for Nuclear Waste Regulatory Analyses, Southwest Research Institute, San Antonio, Texas 78238, USA

^bDepartment of Engineering Science and Mechanics, ^cCenter for Electrochemical Science and Technology, Department of Materials Science and Engineering, The Pennsylvania State University, University Park, Pennsylvania 16802, USA

An impedance model for the electrochemical dissolution of lithium in alkaline solutions is presented. The construction technique of the impedance function depends on calibration to steady-state properties, described in Part II of this series. The model, which is based on the point defect model for the growth and breakdown of passive films, is used to identify effects of various electrolyte solutes on the properties of the lithium film. The high frequency experimental impedance data are explained by the existence of a capacitance that is voltage and frequency dependent, a property that is theoretically rationalized. It is concluded that electrolyte solutes influence the rate of water transport through the outer layer, rate constants, the polarization of the barrier layer/outer layer interface, and the porosity of the outer layer. Based on the shape of predicted impedance signatures, it is suggested that the derived impedance equation may be applicable to other systems.

© 2001 The Electrochemical Society. [DOI: 10.1149/1.1401085] All rights reserved.

Manuscript submitted June 14, 2000; revised manuscript received June 1, 2001. Available electronically August 31, 2001.

Thermodynamic and electrochemical kinetic studies on the lithium/water system demonstrate that the dissolution of the metal under open circuit conditions is regulated by a bilayer film composed of lithium hydride and lithium hydroxide.¹ A steady-state model consistent with this bilayer notion and based on the point defect model (PDM)²⁻⁵ has been developed.^{6,7} The model extends the PDM by incorporating the porous LiOH outer layer and by recognizing the existence of a defective LiH barrier layer. The steady-state model successfully accounts for the rate of metal dissolution and hydrogen evolution in alkaline solutions as functions of the applied voltage. It proposes an outer layer porosity that is a decreasing function of the applied potential, which causes the total current density to be also a decreasing function of the voltage within a certain voltage domain. The steady-state model explains the invariance of the open circuit potential (OCP) in diverse electrolytes and accounts for the variation of the coulombic efficiency with respect to electrolyte composition and voltage, in terms of the compensating effects of the porosity of the outer layer on the partial anodic (Li dissolution) and cathodic current densities.^{6,7}

A more stringent test of the model is performed by measuring the interfacial impedance over a wide frequency domain and comparing the data with calculated impedances as various independent parameters are varied in a systematic manner. In the present paper, the voltage and electrolyte composition are chosen as the relevant independent variables, so as to be consistent with the steady-state electrochemical kinetic work that is reported in Part II of this series.⁶ The present work demonstrates that the modified PDM developed earlier can be extended to explain impedance data.

Theory

Figure 1 summarizes the bilayer model discussed in Part II.⁶ Defective lithium hydride is proposed to exist next to the metal surface and a highly porous lithium hydroxide film, between the LiH layer and the electrolyte. The flux of hydrogen vacancies, V_H^* , from the metal/barrier layer interface (MBI) to the barrier layer/outer layer interface (BOI) is responsible for the growth of the LiH film into the metal. The flux of metal vacancies, V_{Li}^* , in the reverse

direction describes dissolution of the metal. It is believed that cation vacancies, V_{Li}^* , are the main charge carriers in LiH crystals.⁸⁻¹¹ Other studies suggest that anion vacancies and interstitial species play important roles in charge conduction.^{12,13} In the steady-state model, both species transport charge in the LiH film, but cation vacancies appear to be the predominant charge carriers.⁶ Dissolution of the LiH at the BOI together with Li^+ being ejected from the barrier layer cause local supersaturation, and hence, precipitation of the porous LiOH outer layer. The pores remain open in the steady-state, because of the dependence of the chemical potential, and hence solubility of LiOH, on the pore radius.

In this paper, the faradaic impedance of the system is computed by determining the first order perturbation in the total current due to a harmonic perturbation in the applied voltage, as discussed elsewhere.¹⁴⁻¹⁶ By invoking steady-state constraints, an analytical expression for the impedance is computed. Fitting the impedance equation to experimental data permits the estimation of model parameters; thus yielding additional information on the interfacial phenomena that cannot be determined based only on steady-state analyses. The steady-state model derived in Part II⁶ is used as the zero frequency limit. The derived equation for the system impedance is

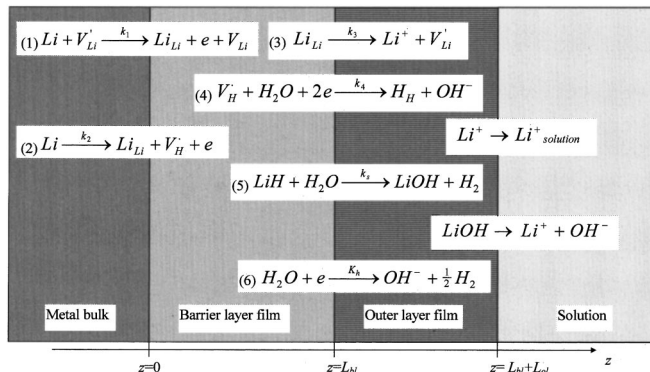


Figure 1. Interfacial reactions leading to generation and annihilation of point defects within the passive film on lithium.

* Electrochemical Society Active Member.

** Electrochemical Society Fellow.

^z E-mail: opensado@swri.org

$$Z = \frac{(1+i)\sqrt{\omega} + B_1}{\left[C_3 + \frac{C_4}{B_1 + (1+i)\sqrt{\omega}} \right] [i(1+i)\omega^{3/2} + B_1 i\omega] + B_2(1+i)\sqrt{\omega} + B_3} + R_s \quad [1]$$

The parameters C_3 , C_4 , B_1 , B_2 , B_3 are defined as functions of various model parameters such as activities, rate constants, transfer and diffusion coefficients, applied potential, and the specific differential capacitance; R_s is a constant, and ω is the frequency. Definitions of C_3 , C_4 , B_1 , B_2 , B_3 for the lithium/water system are described later in this paper. Representation of the system impedance as Eq. 1 is appropriate because it includes a maximal set of five independent parameters that can be obtained via curve fitting to experimental data. In order to derive values for various model parameters, information on the variation of the five parameters with respect to the applied potential, as well as steady-state parameters reported elsewhere,^{6,7} are used. A principal goal of this paper concerns the derivation of Eq. 1 and determination of model parameters.

The total current density derived from charge transfer reactions in Fig. 1 is^{6,7}

$$I_T \approx F \left(\frac{c_{V_{Li}}^{MBI}}{c_o} k_1 + k_2 - 2k_4\theta \frac{c_W^{BOI} c_{V_H}^{BOI}}{c_o^2} - \frac{c_W^{BOI}}{c_o} \theta k_h \right) \\ = F \left(\frac{c_{V_{Li}}^{MBI}}{c_o} k_1 + k_2 + \theta J_W^{BOI} \right) \quad [2]$$

where F is Faraday's constant (9.649×10^4 C mol⁻¹) and k_1 , k_2 , k_4 , k_h are the rate constants for Reactions 1, 2, 4, and 6 in Fig. 1. The concentrations of hydrogen vacancies and lithium ion vacancies in the LiH barrier layer at the BOI (MBI) are symbolized as $c_{V_H}^{BOI}$ and $c_{V_{Li}}^{MBI}$, respectively. The water concentration (molar water flux) in the LiOH pore interior and at the BOI is represented by C_W^{BOI} (J_W^{BOI}). From the charge transfer reactions shown in Fig. 1, the molar flux of water is equal to $-2k_4 c_W^{BOI} c_{V_H}^{BOI} / c_o^2 - k_h c_W^{BOI} / c_o$. The symbol θ represents the porosity of the LiOH layer ($0 \leq \theta \leq 1$). The term θJ_W^{BOI} is interpreted as the molar flux of water averaged over an area that includes both the solid matrix and the pores of the LiOH layer at the BOI.^{17,18}

In deriving the faradaic impedance of the system, besides determining the first order response in I_T due to a small harmonic perturbation in the applied voltage, steady-state constraints are invoked to construct an impedance expression that is consistent with the zero frequency limit. For example, requiring that the rate of film formation is equal to the rate of film dissolution yields⁶

$$k_2 \approx \frac{c_W^{BOI}}{c_o} \theta k_s^o \quad [3]$$

k_s^o symbolizes the standard rate constant of inner layer dissolution (Reaction 5 in Fig. 1). Equation 3 is valid at steady-state, and assumed to be approximately valid under non-steady-state conditions. Substitution of Eq. 3 into Eq. 2, and assuming that $k_1 = k_1^o k_2 / k_2^o$ (in consistency with Part II⁶), yields

$$I_T \approx F \left[\left(\frac{c_{V_{Li}}^{MBI} k_1^o}{c_o k_2^o} + 1 \right) \frac{c_W^{BOI}}{c_o} \theta k_s^o + \theta J_W^{BOI} \right] \quad [4]$$

k_1^o and k_2^o are standard rate constants for Reactions 1 and 2 in Fig. 1. Note that Eq. 2 is valid in general, independent of steady-state constraints. On the other hand, Eq. 4 is expected to be only valid at conditions "close" to steady state, such as those induced by a small

harmonic perturbation in the applied potential of low frequency. According to Eq. 4, the response of the total current, I_T , to a perturbation in the applied potential is defined by the responses of the concentration and flux of water, c_W and J_W , and the outer layer porosity, θ , to that perturbation. These responses are derived below.

The harmonic perturbation to the polarization state, V_o , is represented by

$$V = V_o + \Delta V = V_o + \Delta V_o e^{i\omega t} \quad [5]$$

where V is the total applied potential and ΔV_o is the amplitude of the voltage perturbation. It is understood that only the real part of the complex function $e^{i\omega t}$ has physical significance.

The activity of species j , a_j , is approximated by $a_j \approx c_j / c_o$ (c_j is the molar concentration and c_o , a standard state concentration chosen as 1 M). The constant c_o is used to define activities as dimensionless quantities. Thus, the water activity, a_w , is

$$a_w \approx \frac{c_W}{c_o} \quad [6]$$

The first order response of the water concentration in the pore interior (outer layer), c_W , to the harmonic voltage perturbation can be represented by

$$c_W = c_W^{ss} + \Delta c_W = c_W^{ss} + \Delta c_W^o e^{i\omega t} \quad [7]$$

where c_W^{ss} is the water concentration evaluated at V_o (steady-state concentration) and $\Delta c_W = \Delta c_W^o e^{i\omega t}$ is the resulting harmonic perturbation. In general, in this paper, symbols with an ss (meaning steady-state) superscript denote functions evaluated at V_o . Parameters that are functions of the voltage and not including the ss superscript are understood to be evaluated at V .

Mass conservation dictates that

$$\frac{\partial c_W}{\partial t} = \frac{\partial}{\partial x} D_W \frac{\partial c_W}{\partial x} \quad [8]$$

D_W is the water diffusion coefficient within the pores in the outer layer. Substitution of Eq. 7 into Eq. 8 yields

$$\frac{\partial \Delta c_W}{\partial t} \approx D_W^{ss} \frac{\partial^2 \Delta c_W}{\partial x^2} \quad [9]$$

It can be demonstrated that Eq. 9 is a generally valid first order approximation for the case where D_W is concentration dependent.¹⁹ Correcting terms to Eq. 9 to account for any concentration dependence of D_W are of the order of $(\Delta V_o)^2$, which are negligible in the linear approximation.¹⁹ Substitution of $\Delta c_W = \Delta c_W^o e^{i\omega t}$ into Eq. 9 yields

$$i\omega \Delta c_W^o = D_W^{ss} \frac{\partial^2 \Delta c_W^o}{\partial x^2} \quad [10]$$

The solution to Eq. 10 under the assumption that water transport occurs through a semi-infinite outer layer, that Δc_W is linearly related to the small voltage amplitude ΔV , and satisfying the restriction that the concentration is bounded in the limit $x \rightarrow +\infty$, is

$$c_W = c_W^{ss} + B_W e^{\kappa_W(x-L_{bi})} \Delta V = c_W^{ss} + B_W e^{\kappa_W(x-L_{bi})} \Delta V_o e^{i\omega t} \quad [11]$$

where

$$\kappa_W = -\sqrt{\frac{\omega}{D_W^{ss}}}(1+i) \quad [12]$$

The origin of coordinates for the position variable, x , is set at the MBI (see Fig. 1). B_W is a function of the voltage and frequency and is defined as

$$B_W(V_o, \omega) = \frac{1}{c_o} \frac{\partial c_W}{\partial V} \Big|_{\text{BOI}} \quad [13]$$

Steady-state constraints discussed in Part II are invoked for a more explicit definition of B_W . It has been previously derived that⁶

$$c_W^{ss}|_{\text{BOI}} = \frac{k_2' c_o^2}{k_1' k_s^o c_{V_{\text{Li}}}^{\text{MBI}}} k_3^{ss} \quad [14]$$

k_3^{ss} is the rate constant for Reaction 3 evaluated at V_o . According to Eq. 14, in the limit of zero frequency (*i.e.*, under steady-state conditions)

$$B_W(V_o, 0) = \frac{1}{c_o} \frac{\partial c_W^{ss}}{\partial V} \Big|_{\text{BOI}} = \frac{\alpha_3 \gamma \alpha k_2' c_o}{k_1' k_s^o c_{V_{\text{Li}}}^{\text{MBI}}} k_3^{ss} = \alpha_3 \gamma \alpha \frac{c_W^{ss}|_{\text{BOI}}}{c_o} \quad [15]$$

On the other hand, substitution of Eq. 11 into Ficks' law yields

$$\Delta J_W|_{\text{BOI}} = -D_W^{ss} \frac{\partial \Delta c_W}{\partial x} \Big|_{\text{BOI}} = c_o B_W \sqrt{\frac{D_W^{ss} \omega}{2}} (1+i) \Delta V \quad [16]$$

Necessarily $\Delta J_W|_{\text{BOI}}$ must be bounded in the limit of infinite frequency (a physical requirement); therefore, B_W must decrease with increasing frequency, at least as fast as $\omega^{-1/2}$. Defining B_W as

$$B_W(V_o, \omega) = \frac{\alpha_3 \gamma \alpha k_2' c_o}{k_1' k_s^o c_{V_{\text{Li}}}^{\text{MBI}}} \frac{k_3^{ss}}{1 + A_1(1+i)\sqrt{\omega}} = \frac{\alpha_3 \gamma \alpha \frac{c_W^{ss}|_{\text{BOI}}}{c_o}}{1 + A_1(1+i)\sqrt{\omega}} \quad [17]$$

provides consistent values in the limits of zero and infinite frequency.

In order to assign a physical interpretation to A_1 , let $J_{V\infty}$ symbolize the variation in the flux of water into the porous outer layer with respect to the variation in the applied potential in the limit of infinite frequency; *i.e.*

$$J_{V\infty} = \lim_{\omega \rightarrow \infty} \frac{\partial J_W}{\partial V} \Big|_{\text{BOI}} \quad [18]$$

From Eq. 16 and 17

$$J_{V\infty} \approx \lim_{\omega \rightarrow \infty} \frac{\Delta J_W}{\Delta V} \Big|_{\text{BOI}} = \frac{\alpha_3 \gamma \alpha k_2' c_o^2}{k_1' k_s^o c_{V_{\text{Li}}}^{\text{MBI}}} \frac{k_3^{ss}}{A_1} \sqrt{\frac{D_W^{ss}}{2}} \quad [19]$$

From Eq. 19, it is concluded that

$$A_1 = c_o \frac{\alpha_3 \gamma \alpha k_2' c_o}{k_1' k_s^o c_{V_{\text{Li}}}^{\text{MBI}}} \frac{k_3^{ss}}{J_{V\infty}} \sqrt{\frac{D_W^{ss}}{2}} = \alpha_3 \gamma \alpha \frac{c_W^{ss}|_{\text{BOI}}}{J_{V\infty}} \sqrt{\frac{D_W^{ss}}{2}} \quad [20]$$

In general, $J_{V\infty}$ may be defined as a complex number. However in the present treatment, $J_{V\infty}$ is assumed to be real, which is equivalent to requiring that ΔV and $\Delta J_W|_{\text{BOI}}$ are in phase in the limit of infinite frequency (see Eq. 16). The response of the concentration and flux of water to the voltage perturbation is determined by Eq. 11, 16, 17, and 20. To complete the derivation of the response of the total current, I_T , to the voltage perturbation, the response of the porosity, θ , must be established.

θ is computed by requiring equilibrium in the pore interior between the ionic species, Li^+ and OH^- , and the LiOH matrix. The concentration of Li^+ in the interior of the pore is voltage dependent, implying that θ is also a function of the voltage perturbation. Elsewhere it has been derived that⁶

$$\theta = \frac{P \pi r_o^2}{(\xi_2 + 2\alpha_3 \gamma \alpha V)^2} = \frac{\theta_o}{(\xi_2 + 2\alpha_3 \gamma \alpha V)^2} \quad [21]$$

where P is the number of pores per unit of outer layer surface, and r_o and θ_o ($=P\pi r_o^2$) are a reference length and porosity, respectively. The parameters r_o and ξ_2 are related to the chemical potential of the lithium hydroxide in the pore wall.⁶ The constant α_3 is the transfer coefficient for Reaction 3 (Fig. 1), α is the BOI polarizability,⁶ and γ equals F/RT (R is the ideal gas constant and $T = 298$ K). If it is assumed that Eq. 21 is valid in general, not only at steady state, the perturbation in the porosity, $\Delta\theta$, is

$$\Delta\theta = \frac{\partial \theta}{\partial V} \Big|_{V_o} = \Delta V \frac{4\alpha_3 \gamma \alpha \theta^{ss}}{\xi_2 + 2\alpha_3 \gamma \alpha V_o} \Delta V \quad [22]$$

Equation 21 is valid in general if equilibrium exists between the ions in solution, Li^+ and OH^- , and the LiOH matrix. It is possible that at high frequencies of the perturbation in the potential, Eq. 21 may not hold because of kinetic limitations.

Determination of the response of the total current to the perturbation in the potential is straightforward from results derived above. By differentiation of Eq. 4

$$\Delta I_T \approx F \left[\left(\frac{c_{V_{\text{Li}}}^{\text{MBI}} k_1'}{c_o k_2'} + 1 \right) \left(B_W \theta^{ss} k_s^o \Delta V + \frac{c_W^{ss}|_{\text{BOI}}}{c_o} \Delta\theta k_s^o \right) - \Delta\theta \frac{c_W^{ss}|_{\text{BOI}}}{c_o} (2k_s^o + k_h^{ss}) + \theta^{ss} \Delta J_W^{\text{BOI}} \right] \quad [23]$$

Substitution of Eq. 16 and 22 into Eq. 23 yields

$$\frac{\Delta I_T}{\Delta V} \approx F \alpha_3 \gamma \alpha \frac{c_W^{ss}|_{\text{BOI}}}{c_o} \theta^{ss} k_s^o \left[\frac{4 \left(1 - \frac{c_{V_{\text{Li}}}^{\text{MBI}} k_1'}{c_o k_2'} + \frac{k_h^{ss}}{k_s^o} \right)}{\xi_2 + 2\alpha_3 \gamma \alpha V_o} + \frac{\frac{c_{V_{\text{Li}}}^{\text{MBI}} k_1'}{c_o k_2'} + \frac{c_o}{k_s^o} \sqrt{\frac{D_W^{ss} \omega}{2}} (1+i)}{1 + A_1(1+i)\sqrt{\omega}} \right] \quad [24]$$

It is convenient to express the faradaic admittance of the system as

$$\frac{\Delta I_T}{\Delta V} = \frac{D_1 + D_2(1+i)\sqrt{\omega}}{1 + A_1(1+i)\sqrt{\omega}} \quad [25]$$

where

$$D_1 = F\alpha_3\gamma\alpha \frac{c_{\text{W}}^{\text{ss}}|_{\text{BOI}}}{c_o} \theta^{\text{ss}} k_s^o \left[\frac{4 \left(1 - \frac{c_{\text{V}'\text{Li}}^{\text{MBI}} k_1^{o'}}{c_o k_2^{o'}} + \frac{k_h^{\text{ss}}}{k_s^o} \right)}{\xi_2 + 2\alpha_3\gamma\alpha V_o} \right. \\ \left. + \frac{c_{\text{V}'\text{Li}}^{\text{MBI}} k_1^{o'}}{c_o k_2^{o'}} \right] \quad [26]$$

and

$$D_2 = F\alpha_3\gamma\alpha \frac{c_{\text{W}}^{\text{ss}}|_{\text{BOI}}}{c_o} \theta^{\text{ss}} k_s^o \left[\frac{4 \left(1 - \frac{c_{\text{V}'\text{Li}}^{\text{MBI}} k_1^{o'}}{c_o k_2^{o'}} + \frac{k_h^{\text{ss}}}{k_s^o} \right) A_1}{\xi_2 + 2\alpha_3\gamma\alpha V_o} \right. \\ \left. + \frac{c_o}{k_s^o} \sqrt{\frac{D_{\text{W}}^{\text{ss}}}{2}} \right] \quad [27]$$

Additional steps are needed for the derivation of the system impedance (Eq. 1). If C is the film capacitance, the admittance of the system, Y , is the sum of the faradaic admittance and $i\omega C$; *i.e.*

$$Y = i\omega C + \frac{D_1 + D_2(1+i)\sqrt{\omega}}{1 + A_1(1+i)\sqrt{\omega}} \\ = \frac{CA_1 i(1+i)\omega^{3/2} + i\omega C + D_2(1+i)\sqrt{\omega} + D_1}{1 + A_1(1+i)\sqrt{\omega}} \quad [28]$$

Furthermore, if the solution resistance, R_s , is included, the system impedance is

$$Z = \frac{(1+i)\sqrt{\omega} + B_1}{i(1+i)C\omega^{3/2} + B_1 iC\omega + B_2(1+i)\sqrt{\omega} + B_3} + R_s \quad [29]$$

where B_1 , B_2 , and B_3 are

$$B_1 = \frac{1}{A_1} = \frac{\sqrt{2}J_{\text{V}\infty}}{\alpha_3\gamma\alpha c_{\text{W}}^{\text{ss}}|_{\text{BOI}}\sqrt{D_{\text{W}}^{\text{ss}}}} \quad [30]$$

$$B_2 = \frac{D_2}{A_1} = \frac{\sqrt{2}FJ_{\text{V}\infty}\theta^{\text{ss}}k_s^o}{c_o\sqrt{D_{\text{W}}^{\text{ss}}}} \left[\frac{4 \left(1 - \frac{c_{\text{V}'\text{Li}}^{\text{MBI}} k_1^{o'}}{c_o k_2^{o'}} + \frac{k_h^{\text{ss}}}{k_s^o} \right) A_1}{\xi_2 + 2\alpha_3\gamma\alpha V_o} \right. \\ \left. + \frac{c_o}{k_s^o} \sqrt{\frac{D_{\text{W}}^{\text{ss}}}{2}} \right] \quad [31]$$

$$B_3 = \frac{D_1}{A_1} = \frac{\sqrt{2}FJ_{\text{V}\infty}\theta^{\text{ss}}k_s^o}{c_o\sqrt{D_{\text{W}}^{\text{ss}}}} \left[\frac{4 \left(1 - \frac{c_{\text{V}'\text{Li}}^{\text{MBI}} k_1^{o'}}{c_o k_2^{o'}} + \frac{k_h^{\text{ss}}}{k_s^o} \right)}{\xi_2 + 2\alpha_3\gamma\alpha V_o} \right. \\ \left. + \frac{c_{\text{V}'\text{Li}}^{\text{MBI}} k_1^{o'}}{c_o k_2^{o'}} \right] \quad [32]$$

Because of the steady-state constraints used in deriving Eq. 29, this equation is not valid at sufficiently high frequencies. For that reason, R_s should be interpreted as a constant correcting limitations of the

theory in the limit of infinite frequency. This issue is discussed later in this paper. Parametrization of the impedance as a function of B_1 , B_2 , and B_3 , facilitates fitting the model to the experimental data. Derivation of Eq. 1 from Eq. 29 necessitates a more detailed description of the film capacitance, C .

C is the differential capacitance of the film,¹⁹ which is defined as²⁰

$$C(V_o) = \frac{d\sigma}{dV}\Big|_{V=V_o} = \frac{d(\hat{C}V)}{dV}\Big|_{V=V_o} = \hat{C}(V_o) + V_o \frac{d\hat{C}}{dV}\Big|_{V=V_o} \quad [33]$$

where σ is the surface charge density of the film and $\hat{C}(V_o)$, the specific geometric capacitance (geometric capacitance per unit of surface) evaluated at V_o . Note that, if the specific geometric capacitance, \hat{C} , is independent of the applied potential, the differential capacitance and specific geometric capacitance are equivalent. Equation 33 establishes that perturbations to \hat{C} induced by pertur-

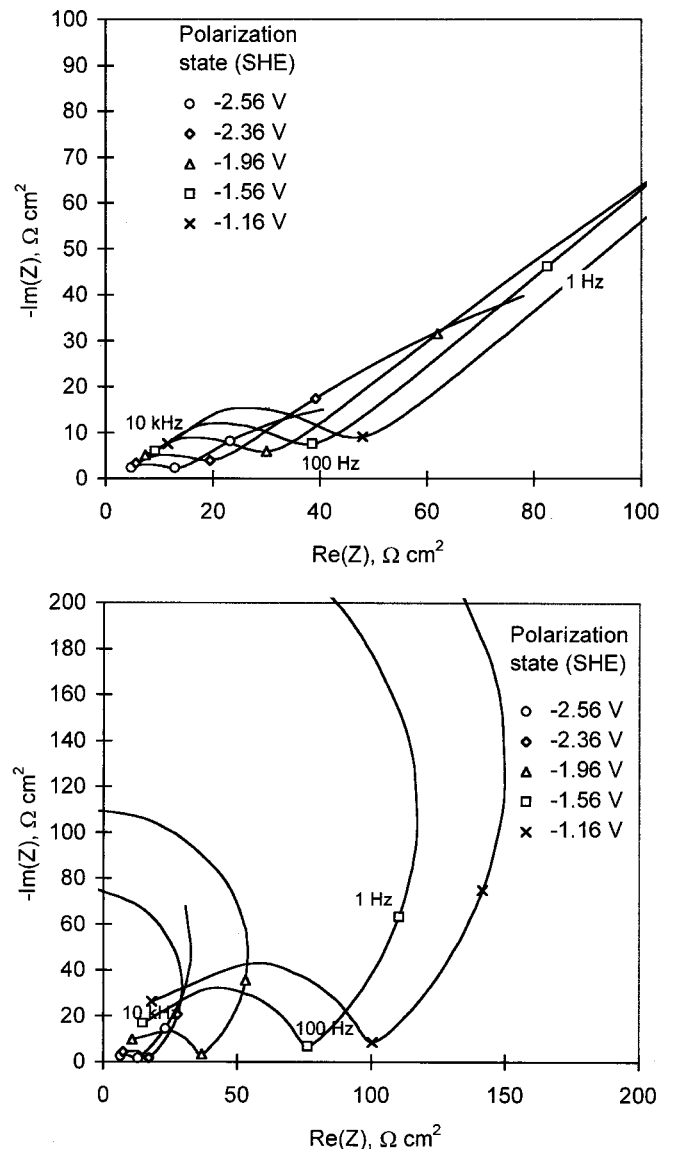


Figure 2. Nyquist plots of electrochemical impedance data. (a) Lithium in 12 M KOH, (b) lithium in 12 M KOH + 0.58 M sucrose. Impedance points at three frequencies (10 kHz, 100 Hz, 1 Hz) have been indicated for each data set. Data for five bias voltages with respect to SHE are included.

Table I. Parameter values and confidence intervals minimizing the error function, Eq. 1, applied to the 12 M KOH electrolyte system. The percentages represent cumulative distribution function percents (*i.e.*, percent quantiles) and the standard deviation (sd) of the bootstrap data.^a The statistics for D_1 and D_2 were obtained from the bootstrap data for B_1 , B_2 , and B_3 .

V_{SHE}	$C_3/(10^{-6} \text{ s } \Omega^{-1} \text{ cm}^{-2})$					$C_4/(10^{-4} \text{ s}^{1/2} \Omega^{-1} \text{ cm}^{-2})$				
V_{SHE}	1%	50%	99%	mean	sd	1%	50%	99%	mean	sd
-2.56	-0.82	7.62	25.60	9.63	6.14	7.4	16.49	27.51	16.94	4.77
-2.36	0.03	8.62	20.10	9.57	4.35	2.1×10^{-8}	10.13	21.28	10.55	4.72
-1.96	1.76	6.90	20.03	7.78	4.06	0.4	4.26	7.47	4.38	2.04
-1.56	0.38	5.58	13.20	5.42	2.25	8.7×10^{-14}	2.39	7.58	2.45	1.50
-1.16	1.20	4.91	10.95	4.71	1.80	0.012	1.40	4.61	1.60	1.06
		$B_1/(s^{-1/2})$					$B_2/(10^{-2} \Omega^{-1} \text{ cm}^{-2})$			
V_{SHE}	1%	50%	99%	mean	sd	1%	50%	99%	mean	sd
-2.56	2.37	6.60	12.52	7.11	1.81	6.37	8.59	10.55	8.63	0.89
-2.36	2.02	13.83	26.38	13.63	4.44	3.05	6.10	8.95	6.16	1.08
-1.96	2.76	16.80	43.80	19.10	8.47	3.65	4.37	6.53	4.46	0.63
-1.56	3.02	19.69	49.20	20.15	6.74	2.44	3.53	5.68	3.59	0.35
-1.16	3.24	23.21	40.00	24.25	7.88	2.77	2.85	3.56	3.01	0.25
		$B_3/(s^{-1/2} \Omega^{-1} \text{ cm}^{-2})$					$R_s/(\Omega \text{ cm}^2)$			
V_{SHE}	1%	50%	99%	mean	sd	1%	50%	99%	mean	sd
-2.56	-2.2×10^{-2}	3.4×10^{-4}	5.2×10^{-2}	4.7×10^{-3}	1.2×10^{-2}	2.52	3.20	5.88	3.45	0.72
-2.36	-1.5×10^{-2}	-2×10^{-17}	-9.1×10^{-19}	-7.6×10^{-4}	2.6×10^{-3}	3.08	4.58	9.66	5.08	1.52
-1.96	-4.6×10^{-3}	-3.8×10^{-12}	-1.3×10^{-18}	-3.2×10^{-4}	9.6×10^{-4}	3.38	5.92	13.82	6.76	2.45
-1.56	-6.1×10^{-2}	-3.9×10^{-3}	-5×10^{-18}	-1.0×10^{-2}	1.4×10^{-2}	3.28	7.14	16.04	7.50	2.10
-1.16	-8.4×10^{-3}	-7.4×10^{-16}	-5.8×10^{-17}	-2.7×10^{-4}	1.3×10^{-3}	6.91	10.24	23.23	11.43	3.69
		$D_1/(\Omega^{-1} \text{ cm}^{-1})$					$D_2/(10^{-3} \text{ s}^{1/2} \Omega^{-1} \text{ cm}^{-2})$			
V_{SHE}	1%	50%	99%	mean	sd	1%	50%	99%	mean	sd
-2.56	-3.3×10^{-3}	3.7×10^{-5}	1.3×10^{-2}	8.2×10^{-4}	2.4×10^{-3}	7.20	12.53	40.38	13.02	4.83
-2.36	-7.7×10^{-4}	-1.9×10^{-18}	-8.4×10^{-20}	-4.8×10^{-5}	1.6×10^{-4}	2.92	4.60	29.69	5.18	3.68
-1.96	-1.8×10^{-4}	-1.7×10^{-13}	-3.1×10^{-20}	-1.6×10^{-5}	4.3×10^{-5}	1.49	2.35	16.03	3.04	2.85
-1.56	-3.5×10^{-3}	-1.8×10^{-4}	-2.6×10^{-19}	-6×10^{-4}	8.4×10^{-4}	1.05	1.76	11.05	2.09	1.43
-1.16	-3.3×10^{-4}	-5.5×10^{-17}	-2.4×10^{-18}	-1.1×10^{-5}	5.3×10^{-5}	0.80	1.25	8.63	1.49	1.19

^a See main text for a detailed definition of bootstrap data. Bootstrap data were derived by applying the parametric bootstrap technique²⁴ to define confidence intervals.

Table II. Parameter values and confidence intervals minimizing the error function, Eq. 1, applied to the 12 M KOH and 0.58 M sucrose electrolyte system. The percentages represent cumulative distribution function percents (*i.e.*, percent quantiles) and the standard deviation (sd) of the bootstrap data. The statistics for D_1 and D_2 were obtained from the bootstrap data for B_1 , B_2 , and B_3 .

V_{SHE}	$C_3/(10^{-6} \text{ s } \Omega^{-1} \text{ cm}^{-2})$					$C_4/(10^{-5} \text{ s}^{1/2} \Omega^{-1} \text{ cm}^{-2})$				
V_{SHE}	1%	50%	99%	mean	sd	1%	50%	99%	mean	sd
-2.56	0.10	10.31	23.00	10.54	5.41	2.3×10^{-14}	53.07	127.37	56.77	33.00
-2.36	1.69	10.88	20.96	10.05	4.02	9.6×10^{-15}	0.89	44.68	3.91	8.90
-1.96	1.54	4.20	8.47	4.39	1.39	2.6×10^{-14}	0.07	3.26	0.32	0.62
-1.56	1.06	2.36	5.46	2.67	1.05	2.9×10^{-14}	10^{-12}	0.39	0.02	0.08
-1.16	0.64	1.74	3.50	1.78	0.54	2.6×10^{-14}	0.06	2.58	0.38	0.60
		$B_1/(s^{-1/2})$					$B_2/(10^{-2} \Omega^{-1} \text{ cm}^{-2})$			
V_{SHE}	1%	50%	99%	mean	sd	1%	50%	99%	mean	sd
-2.56	2.75	18.34	43.38	18.02	7.45	12.96	13.96	22.80	14.90	2.18
-2.36	2.48	16.13	35.08	16.06	6.92	10.08	11.11	12.62	11.16	0.57
-1.96	1.11	6.91	19.20	7.24	4.14	3.42	3.86	4.62	3.88	0.26
-1.56	0.98	6.79	15.86	6.55	3.00	1.58	1.69	1.91	1.70	0.09
-1.16	0.81	4.71	12.01	5.22	2.28	1.16	1.23	1.37	1.24	0.05
		$B_3/(10^{-2} \text{ s}^{-1/2} \Omega^{-1} \text{ cm}^{-2})$					$R_s/(\Omega \text{ cm}^2)$			
V_{SHE}	1%	50%	99%	mean	sd	1%	50%	99%	mean	sd
-2.56	-38.93	-23.70	-3.00	-24.16	8.10	3.47	4.28	5.87	4.35	0.46
-2.36	-52.36	-29.88	-3.84	-28.52	8.80	4.15	5.29	6.72	5.36	0.46
-1.96	-22.89	-12.72	-1.72	-13.57	4.32	5.49	6.65	9.80	6.93	1.02
-1.56	-8.14	-5.30	-0.64	-5.34	1.54	8.03	9.84	14.48	10.47	1.98
-1.16	-5.32	-3.21	-0.46	-3.23	1.06	5.65	9.69	20.68	10.65	3.06
		$D_1/(10^{-2} \Omega^{-1} \text{ cm}^{-1})$					$D_2/(10^{-3} \text{ s}^{1/2} \Omega^{-1} \text{ cm}^{-2})$			
V_{SHE}	1%	50%	99%	mean	sd	1%	50%	99%	mean	sd
-2.56	-2.50	-1.48	-0.21	-1.43	0.44	3.57	8.46	47.07	9.95	6.48
-2.36	-2.81	-1.81	-1.22	-1.89	0.38	3.60	6.93	40.68	8.69	5.74
-1.96	-4.75	-2.01	-1.19	-2.26	0.98	2.41	5.50	32.00	7.55	5.29
-1.56	-2.04	-0.81	-0.51	-0.91	0.37	1.20	2.51	16.30	3.49	2.93
-1.16	-1.44	-0.64	-0.44	-0.66	0.20	1.12	2.54	14.36	2.95	1.98

Table III. Steady-state parameters from Ref. 6 and 7.

Term no.	Term	Value
1	$\alpha_h \alpha$	0.08
2	$\alpha_3 \alpha$	0.012
3	ξ_2	3.86
4	$k_1^{o'} c_{V_L}^{MBI} / k_2^{o'} c_o$	18.2
5	$e^{-\alpha_h \gamma (\beta \text{pH}_{\text{BOI}} + \phi_{\text{BOI}}^o + \alpha \phi_R)} k_h^{o'} / k_s^o$	2.2×10^{-3}

bations in the applied potential have an effect on the differential capacitance and on the system impedance (see Eq. 29). In general, perturbations in \hat{C} may be frequency dependent as argued in the following.

For a parallel plate capacitor, the geometric capacitance is inversely proportional to the distance separating the plates. Thus, it is reasonable to assume that \hat{C} is a function of the barrier layer (hydride film) thickness, L_{bl} , and the applied potential; *i.e.*

$$\hat{C} = \hat{C}(V, L_{\text{bl}}) \quad [34]$$

Steady-state and PDM indicate that the potential drop at the MBI, ϕ_{MBI} , is computed as⁶

$$\phi_{\text{MBI}} = (1 - \alpha)(V + \phi_R) - \beta \text{pH}_{\text{BOI}} - \phi_{\text{BOI}}^o - \varepsilon L_{\text{bl}} \quad [35]$$

ϕ_R is a reference potential, β and ϕ_{BOI}^o are constants with units of voltage, pH_{BOI} is the pH at the BOI, and ε is the average electric field in the LiH layer. The rate constant, k_2 , depends on ϕ_{MBI} as⁶

$$k_2 = k_2^{o'} e^{\alpha_2 \gamma \phi_{\text{MBI}}} \quad [36]$$

Equations 3, 35, and 36 yield

$$L_{\text{bl}} = \frac{1 - \alpha}{\varepsilon} V - \frac{\beta}{\varepsilon} \text{pH}_{\text{BOI}} - \frac{1}{\varepsilon} \phi_{\text{BOI}}^o + \frac{1 - \alpha}{\varepsilon} \phi_R - \frac{1}{\alpha_2 \gamma \varepsilon} \ln \left(\frac{k_s^o}{k_2^{o'}} \right) - \frac{1}{\alpha_2 \gamma \varepsilon} \ln \theta - \frac{1}{\alpha_2 \gamma \varepsilon} \ln \frac{c_{\text{W}}^{\text{BOI}}}{c_o} \quad [37]$$

The response of the barrier layer thickness to the voltage perturbation is obtained by differentiation of Eq. 37; *i.e.*

$$\Delta L_{\text{bl}} = \left[(1 - \alpha) \alpha_2 + \frac{4 \alpha_3 \alpha}{\xi_2 + 2 \alpha_3 \gamma \alpha V_o} - \frac{\alpha_3 \alpha}{1 + A_1 (1 + i) \sqrt{\omega}} \right] \frac{\Delta V}{\alpha_2 \varepsilon} \quad [38]$$

consequently

$$V_o \frac{d\hat{C}}{dV} \Big|_{V_o} \approx V_o \frac{\partial \hat{C}}{\partial V} \Big|_{V_o} + V_o \frac{\partial \hat{C}}{\partial L_{\text{bl}}} \Big|_{V_o} \frac{\Delta L_{\text{bl}}}{\Delta V} = C_1(V_o) + \frac{C_2(V_o)}{A_1 [B_1 + (1 + i) \sqrt{\omega}]} \quad [39]$$

C_1 and C_2 are two unknown functions of the applied voltage. Note that Eq. 39 is valid in general if $\hat{C} = \hat{C}(V, c_{\text{W}}^{\text{BOI}})$. From Eq. 33 and 39, it is concluded that the differential capacitance, C , is of the form

$$C = C_3(V_o) + \frac{C_4(V_o)}{B_1 + (1 + i) \sqrt{\omega}} \quad [40]$$

In the present approach, C_3 and C_4 are treated as unknown functions of the applied voltage, to be determined via a curve fitting technique.

Equation 1 is readily derived from Eq. 29 and 40. Excellent agreement between experimental data and the impedance function in Eq. 1 has been found, as discussed later in this paper.

Experimental

Experimental impedance data were gathered as part of a program to develop lithium/water batteries.^{21,22} The electrochemical cell used for acquiring the impedance data included lithium (99% purity) as the working electrode, a saturated calomel electrode (SCE)/Luggin probe, and a nickel gauze (a mesh woven from 0.114 mm diam wire) counter electrode as described in Part II.⁶ Lithium was mounted in a Teflon sample holder of cylindrical shape, which defined the area of the lithium surface (0.95 cm²) that was exposed to the electrolyte. The tip of the reference electrode (Luggin probe) was placed near the surface of the working electrode to minimize the potential drop due to the electrolyte resistance. The nickel gauze counter electrode was placed 5 cm apart from the working electrode. In order to reduce interference from external sources, the electrochemical cell was located within a Faraday cage. Impedance data were gathered in 12 M KOH electrolytes with and without sucrose (0.58 M). Experiments at lower concentrations are not feasible because of the high

Table IV. Parameter ranges and derivation method.

Term no.	Term	Ranges		Derivation Method
		12 M KOH	12 M KOH+0.58 M sucrose	
1	$k_3^{o'} e^{\alpha_3 \gamma (\beta \text{pH}_{\text{HOI}} + \phi_{\text{BOI}}^o + \alpha \phi_R)} \theta_o$	1.5×10^{-20} 1.7×10^{-7} mol/(cm ² s)	2.7×10^{-6} 6.4×10^{-6} mol/(cm ² s)	Fitting the right side of Eq. 43 to 1 and 99 percent quantile data for D_1 (Tables I and II) times the factor in Eq. 42, as a function of the applied potential.
2	$\frac{c_o}{k_s^o} \sqrt{\frac{D_{\text{W}}^{\text{SS}}}{2}}$	25.9, $7.8 \times 10^{15} \text{ s}^{-1/2}$	2.3, 78.1 s ^{1/2}	From Eq. 27, data in Table III, bootstrap data for D_2 , and the bound values for term 1, bootstrap data for term 2 were calculated. The upper (lower) value of term 1 was used to determine the lower (upper) bound for term 2, by computing the maximum (minimum) of bootstrap data for term 2.
3	$\frac{J_{V_{\infty}}}{k_3^{o'} e^{\alpha_3 \gamma (\beta \text{pH}_{\text{BOI}} + \phi_{\text{BOI}}^o + \alpha \phi_R)}}$	5.4 $2.3 \times 10^{14} \text{ V}^{-1}$	0.5, 2.1 V ⁻¹	From Eq. 20 and the bootstrap data for term 2, two sets of bootstrap data for term 3 were calculated. The lower (upper) bound is the minimum (maximum) of these bootstrap data.
4	ξ_1	474 mA/cm ²	200 mA/cm ²	Reported in Ref. 6 and 7 or extrapolated from data therein.
5	$(\alpha_3 + \alpha_h)(\beta \text{pH}_{\text{BOI}} + \phi_{\text{BOI}}^o + \alpha \phi_R)$	-0.86, -0.086 V	0.007, 0.029 V	Derived from Eq. 46 and bound values for term 1.

Table V. Ranges for physical quantities derived from data in Tables III and IV by assuming that $\alpha = 0.5$.

Term no.	Term	Ranges		Interpretation
		12 M KOH	12 M KOH + 0.58 M sucrose	
1	$k_3^{o'} \theta_o$	$2.3 \times 10^{-20}, 1.34 \times 10^{-5}$ mol/(cm ² s)	$2.3 \times 10^{-6}, 6.2 \times 10^{-6}$ mol/(cm ² s)	Higher porosity or faster injection of lithium cations into the solution for the 12 M KOH + 0.58 M sucrose electrolyte system.
2	$\frac{c_o}{k_s} \sqrt{\frac{D_W^{ss}}{2}}$	$25.9, 7.8 \times 10^{15} \text{ s}^{-1/2}$	$2.3, 78.1 \text{ s}^{1/2}$	Higher rate of water transport through the pores in the LiOH outer layer in the 12 M KOH electrolyte system.
3	$\frac{J_{V\infty}}{k_3^{o'}}$	$5.4, 2.3 \times 10^{14} \text{ V}^{-1}$	$0.52, 2.4 \text{ V}^{-1}$	Faster injection of lithium cations into the solution for the 12 M KOH + 0.58 M sucrose electrolyte system (see term 1) and/or faster rate of water consumption for the 12 M KOH electrolyte system.
4	$\frac{K_h^{o'}}{k_s^{o'}}$	$5.1 \times 10^{-16}, 1.2 \times 10^{-4}$	$1.7 \times 10^{-3}, 5.9 \times 10^{-3}$	Faster rate of LiH dissolution rate for 12 M KOH electrolyte system or faster rate of water reduction for the 12 M KOH + 0.58 M sucrose electrolyte system.

reactivity of the system. Data were collected by varying the frequency over a range of 0.05 Hz to 20 kHz. The amplitude of the perturbation to the applied potential was 8 mV. Impedance data were measured at different lithium polarization potentials: $-1.16, -1.56, -1.96, -2.36,$ and $-2.56 \text{ V}_{\text{SHE}}$. The polarization potential was applied for 5 min prior to the data collection. This pretreatment was intended to increase the stability of the system.

Results and Discussion

Figure 2 shows Nyquist plots [imaginary ($-Z$) vs. real (Z), Z = impedance] of electrochemical impedance data. Figures 2a and b display impedance data for 12 M KOH and 12 M KOH + 0.58 M sucrose electrolytes, respectively, for different polarization states (vs. standard hydrogen electrode, SHE). The high frequency data plotted in Fig. 2 exhibit interesting features. The impedance of any charge transfer process coupled to a constant (i.e., independent of frequency) differential capacitance yields a perfect semicircle in the Nyquist plane.²³ Therefore, the high frequency region in Fig. 2b is more consistent with a constant differential capacitance than is the high frequency loci in Fig. 2a, with the form

of the latter being classically accounted for by distributed relaxation time constants or the presence of constant phase elements in an electrical analog.

The angles of the low frequency impedance loci in Fig. 2a are $\sim \pi/4$ and suggest a diffusion impedance of the Warburg kind,²³ as might be expected for a semi-infinite diffusion process (related to the water transport through the outer layer). The low frequency loci in Fig. 2b points to a negative intersection on the real axis in the limit of zero frequency. Equivalent circuits can reproduce this behavior with the presence of a negative resistance, whose existence is not justified in linear system circuit theory. However, this negative resistance is readily explained electrochemically. The slope of the total current density vs. voltage, dI_T^{ss}/dV , in Fig. 4a and 5a in part II⁶ is negative for potentials above $-2.5 \text{ V}_{\text{SHE}}$. The derivative dI_T^{ss}/dV is the steady-state differential faradaic admittance. In the limit of zero frequency (i.e., at steady state), the total admittance is equal to the faradaic admittance, thus explaining the low frequency trends in Fig. 2b. The impedance loci in Fig. 2a could also exhibit negative intersections on the real axis at zero frequency. This is not readily observed, as the steady-state differential faradaic admittance,

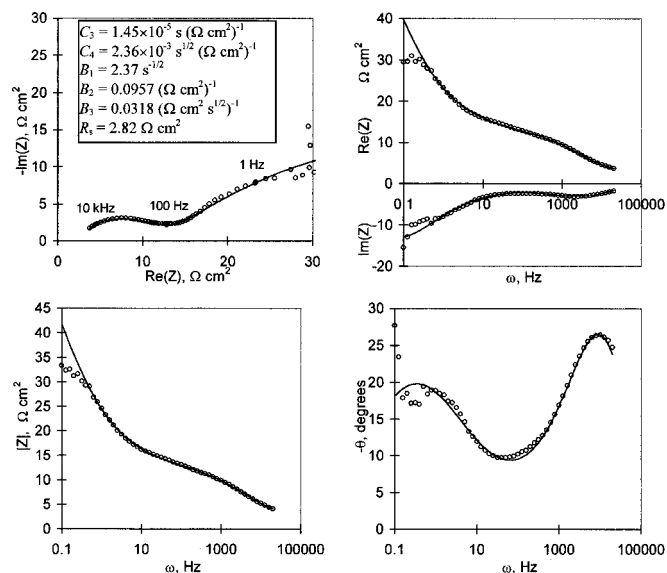


Figure 3. Nyquist and Bode plots of impedance data for lithium polarized at $-2.56 \text{ V}_{\text{SHE}}$ in a 12 M KOH electrolyte. Experimental data are represented by circles. Points at three frequencies are highlighted in the Nyquist plot. The best fit parameters, used in the computation of the solid lines, are indicated in the framed box.

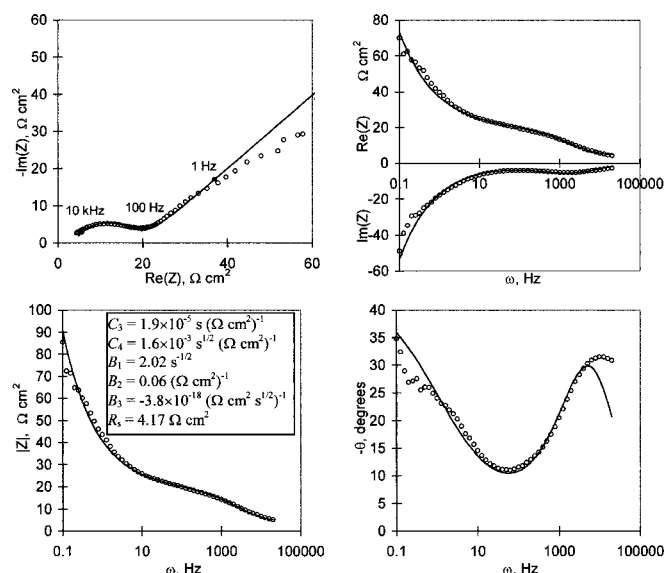


Figure 4. Nyquist and Bode plots of impedance data for lithium polarized at $-2.36 \text{ V}_{\text{SHE}}$ in a 12 M KOH electrolyte. Experimental data are represented by circles. Points at three frequencies are highlighted in the Nyquist plot. The best fit parameters, used in the computation of the solid lines, are indicated in the framed box.

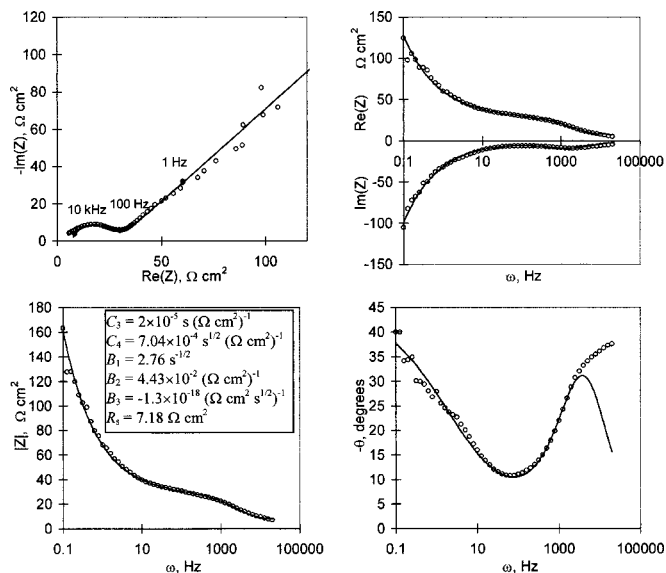


Figure 5. Nyquist and Bode plots of impedance data for lithium polarized at $-1.96 V_{SHE}$ in a 12 M KOH electrolyte. Experimental data are represented by circles. Points at three frequencies are highlighted in the Nyquist plot. The best fit parameters, used in the computation of the solid lines, are indicated in the framed box.

dI_T^{SS}/dV , is close to zero and because of the difficulty in probing the system at sufficiently low frequencies.

The impedance parameters in Eq. 1 were determined by minimizing an error function defined as

$$\text{error} = \sum_{\omega} (|\text{Re}(Z) - \text{Re}(Z_e)| + |\text{Im}(Z) - \text{Im}(Z_e)|) \quad [41]$$

where Z is the impedance computed with Eq. 1 and Z_e , the experimental impedance. The sum in Eq. 41 includes all of the experimentally accessible frequencies (from 0.1 Hz to 20 kHz). The objective

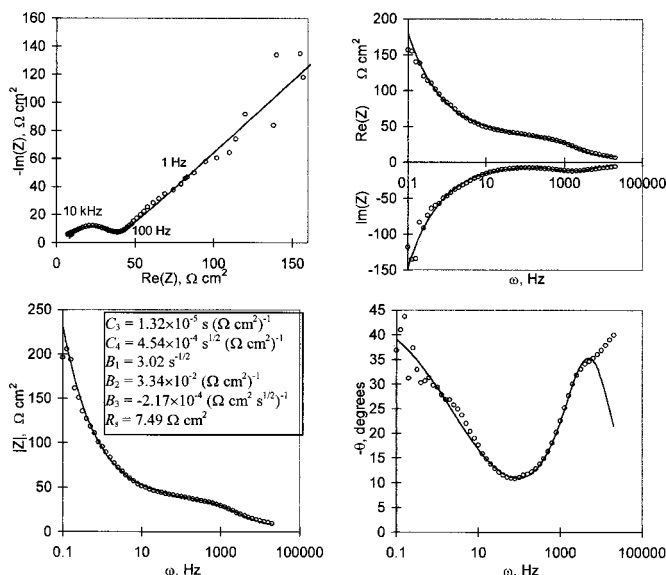


Figure 6. Nyquist and Bode plots of impedance data for lithium polarized at $-1.56 V_{SHE}$ in a 12 M KOH electrolyte. Experimental data are represented by circles. Points at three frequencies are highlighted in the Nyquist plot. The best fit parameters, used in the computation of the solid lines, are indicated in the framed box.

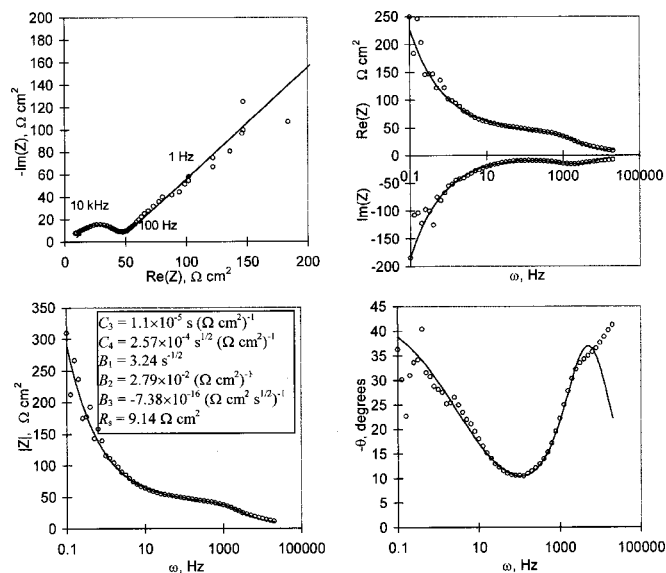


Figure 7. Nyquist and Bode plots of impedance data for lithium polarized at $-1.16 V_{SHE}$ in a 12 M KOH electrolyte. Experimental data are represented by circles. Points at three frequencies are highlighted in the Nyquist plot. The best fit parameters, used in the computation of the solid lines, are indicated in the framed box.

function, Eq. 41, was preferred over a standard squared expression because minimization of this latter function produced in general poor fits to the high frequency impedance. On the other hand, minimization of the objective function in Eq. 41 usually yielded more balanced results, with adequate fits to both the low and high frequency data.

The error function, Eq. 41, was minimized as a function of C_3 , C_4 , B_1 , B_2 , B_3 , and R_s , by a steepest descent algorithm (a numerical Newton algorithm readily available in Mathematica 4.0). Confidence intervals for the parameters were estimated by a variant of the technique known as parametric bootstrap.²⁴ In this technique,

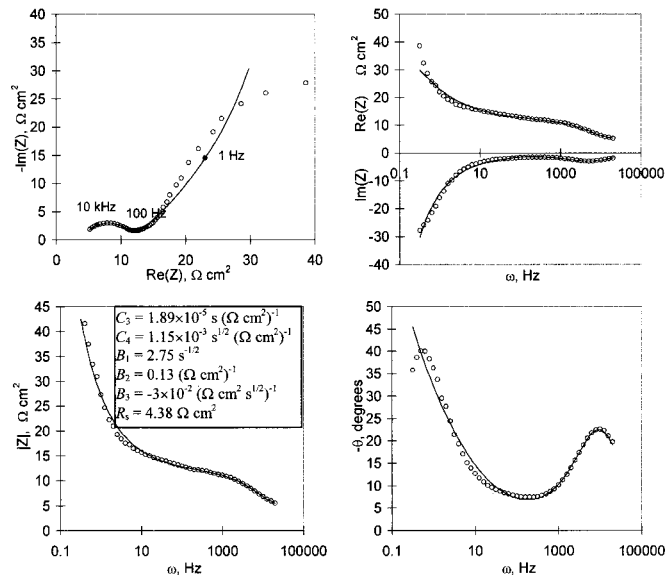


Figure 8. Nyquist and Bode plots of impedance data for lithium polarized at $-2.56 V_{SHE}$ in a 12 M KOH + 0.58 M sucrose electrolyte. Experimental data are represented by circles. Points at three frequencies are highlighted in the Nyquist plot. The best fit parameters, used in the computation of the solid lines, are indicated in the framed box.

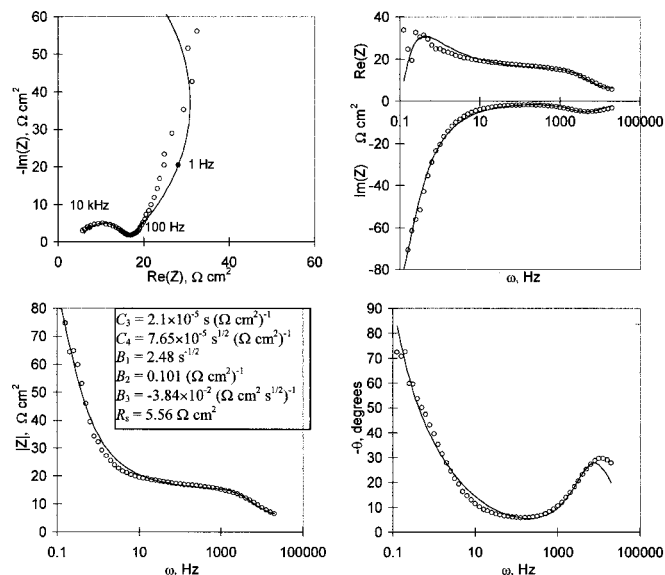


Figure 9. Nyquist and Bode plots of impedance data for lithium polarized at $-2.36 V_{SHE}$ in a 12 M KOH + 0.58 M sucrose electrolyte. Experimental data are represented by circles. Points at three frequencies are highlighted in the Nyquist plot. The best fit parameters, used in the computation of the solid lines, are indicated in the framed box.

an impedance set (defined as a collection of impedance data at a given polarization potential and electrolyte composition) was transformed into one hundred sets by random selection, without repetition, of impedance points in the original set. For each of these one hundred sets, parameters C_3 , C_4 , B_1 , B_2 , B_3 , and R_s were derived via minimization of Eq. 41, yielding one hundred values for each of the parameters, and allowing for the computation of statistics and definition of confidence intervals reported in Tables I and II. In this paper, data generated for each of the parameters via the bootstrap technique is referred to as bootstrap data. Data derived from manipulation (*i.e.*, multiplication, division, etc.) of bootstrap data is

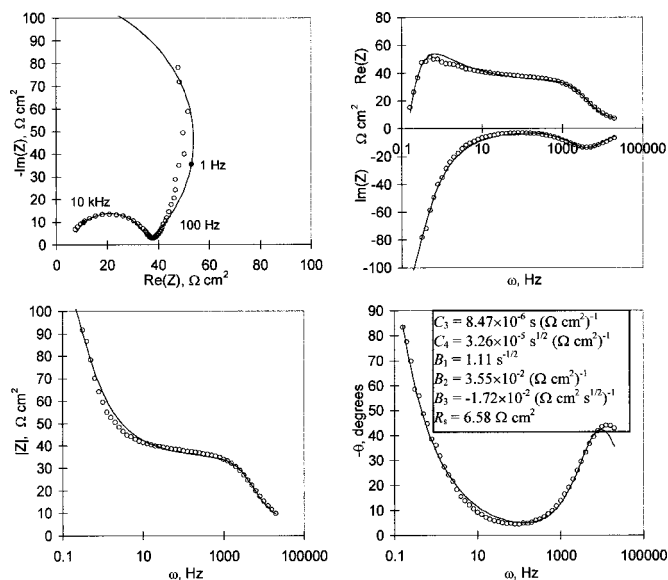


Figure 10. Nyquist and Bode plots of impedance data for lithium polarized at $-1.96 V_{SHE}$ in a 12 M KOH + 0.58 M sucrose electrolyte. Experimental data are represented by circles. Points at three frequencies are highlighted in the Nyquist plot. The best fit parameters, used in the computation of the solid lines, are indicated in the framed box.

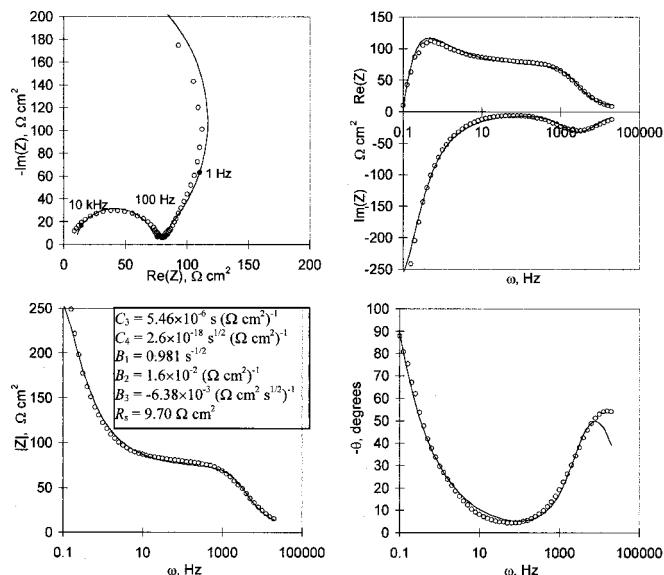


Figure 11. Nyquist and Bode plots of impedance data for lithium polarized at $-1.56 V_{SHE}$ in a 12 M KOH + 0.58 M sucrose electrolyte. Experimental data are represented by circles. Points at three frequencies are highlighted in the Nyquist plot. The best fit parameters, used in the computation of the solid lines, are indicated in the framed box.

also referred to as bootstrap data. The number one hundred was selected to make the problem computationally tractable and also because statistics from one hundred samples were not significantly different from those derived with two hundred sets, for a few testing cases. Tables I and II also contain statistics for the parameters D_1 and D_2 , determined from bootstrap data for B_1 , B_2 , and B_3 , since $D_1 = B_3/B_1$, and $D_2 = B_2/B_1$ (see Eq. 30-32). The method of derivation of physical parameters as functions of the statistics in Tables I and II and bootstrap data is discussed as follows.

Based on the data in Table III (steady-state results from Ref. 6 and 7)

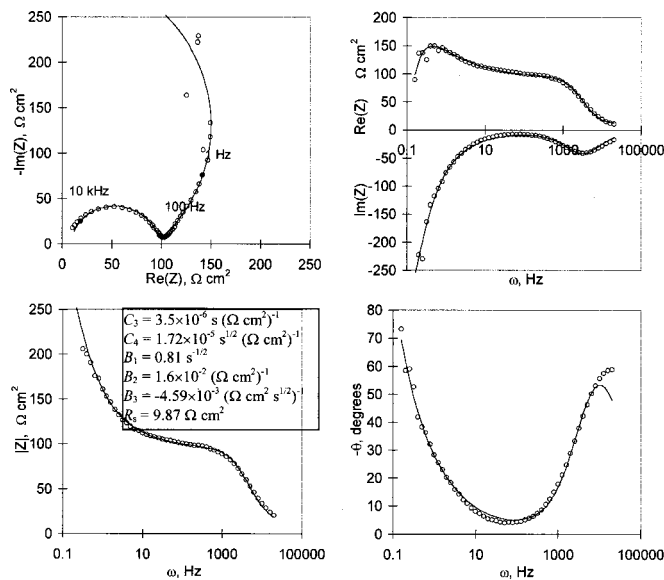


Figure 12. Nyquist and Bode plots of impedance data for lithium polarized at $-1.16 V_{SHE}$ in a 12 M KOH + 0.58 M sucrose electrolyte. Experimental data are represented by circles. Points at three frequencies are highlighted in the Nyquist plot. The best fit parameters, used in the computation of the solid lines, are indicated in the framed box.

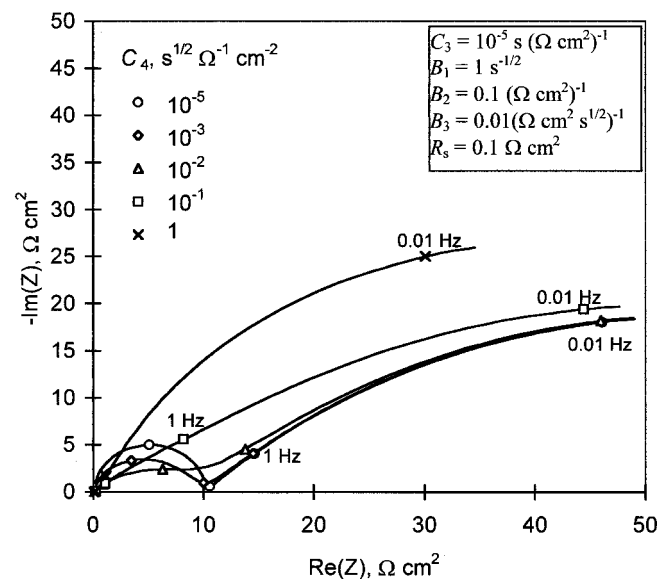
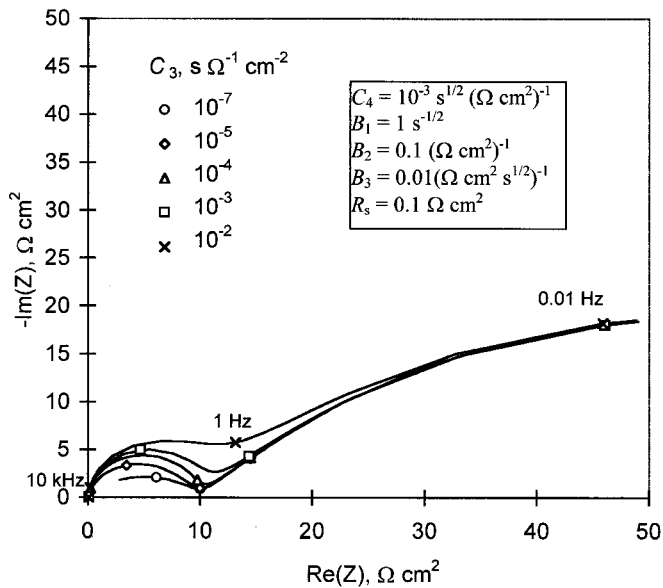
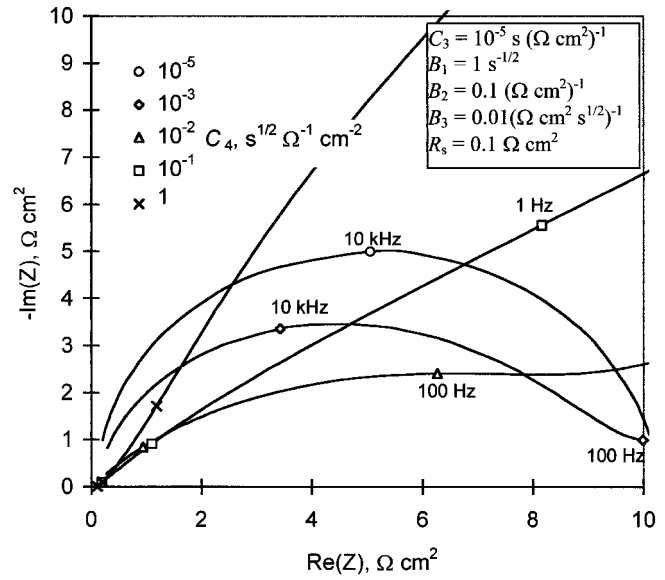
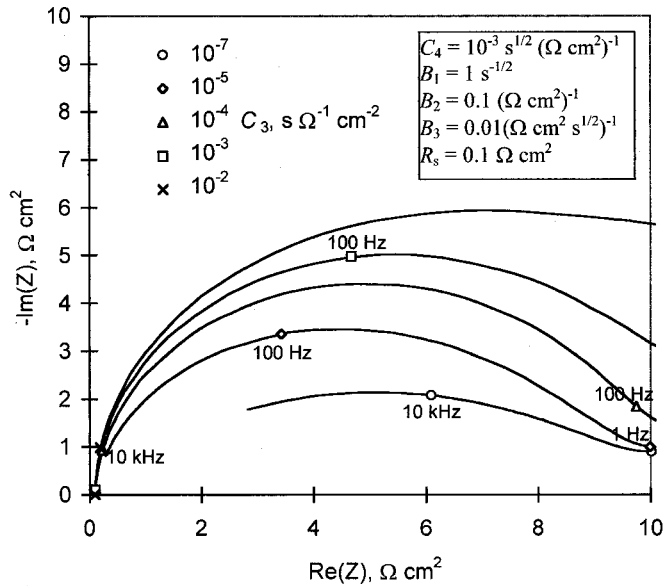


Figure 13. Nyquist plots for two different frequency ranges of the impedance function. C_3 is varied in the range 10^{-7} to $10^{-2} \text{ s } \Omega^{-1} \text{ cm}^{-2}$. Values of the remaining parameters are indicated in the box. Impedance data at four frequencies (0.01 Hz, 1 Hz, 100 Hz, and 10 kHz) are indicated for each case, but only few of these points have been labeled.

Figure 14. Nyquist plots for two different frequency ranges of the impedance function. C_4 is varied in the range 10^{-5} to $1 \text{ s}^{1/2} \Omega^{-1} \text{ cm}^{-2}$. Values of the remaining parameters are indicated in the box. Impedance data at four frequencies (0.01 Hz, 1 Hz, 100 Hz, and 10 kHz) are indicated for each case, but only few of these points have been labeled.

$$\frac{k_1^{o'} c_{V_{Li}}^{MBI}}{k_2^{o'} c_o \alpha_3 \alpha \gamma F} = 4.04 \times 10^{-4} \frac{\text{mol}}{\text{cm}^2 \text{ s}} \quad [42]$$

Multiplication of Eq. 26 by the left side of Eq. 42 yields

$$\frac{k_1^{o'} c_{V_{Li}}^{MBI}}{k_2^{o'} c_o \alpha_3 \alpha \gamma F} D_1 = \theta^{ss} k_3^{ss} \left[\frac{4 \left(1 - \frac{c_{V_{Li}}^{MBI} k_1^{o'}}{c_o k_2^{o'}} + \frac{k_h^{ss}}{k_s^{ss}} \right)}{\xi_2 + 2\alpha_3 \gamma \alpha V_o} + \frac{c_{V_{Li}}^{MBI} k_1^{o'}}{c_o k_2^{o'}} \right] \quad [43]$$

In deriving Eq. 43, the steady-state relationship in Eq. 14 was used. Data in Tables I and II and the numerical factor in Eq. 42 were used in determining numerical values for the left side of Eq. 43. Table III contains the majority of the terms in the right side of Eq. 43. Those

that are not contained in Table III were obtained by fitting Eq. 43 to the numerical data as a function of the potential, by a method outlined below.

The rates k_3^{ss} and k_h^{ss} are defined as functions of the applied potential as^{6,7}

$$k_3^{ss} = k_3^{o'} e^{\alpha_3 \gamma (\beta \text{pH}_{\text{BOI}^+} + \phi_{\text{BOI}^+}^{o'} + \alpha \phi_R)} e^{-\alpha_3 \gamma \alpha V_o} \quad [44]$$

and

$$k_h^{ss} = k_h^{o'} e^{-\alpha_h \gamma (\beta \text{pH}_{\text{BOI}^+} + \phi_{\text{BOI}^+}^{o'} + \alpha \phi_R)} e^{-\alpha_h \gamma \alpha V_o} \quad [45]$$

By substitution of Eq. 44, 45, and 21 into Eq. 43, and with comparison to the steady-state parameters in Table III, it is evident that one degree of freedom, by the combined term $k_3^{o'} e^{\alpha_3 \gamma (\beta \text{pH}_{\text{BOI}^+} + \phi_{\text{BOI}^+}^{o'} + \alpha \phi_R)} \theta_o$, is available to describe the variation of $k_1^{o'} c_{V_{Li}}^{MBI} D_1 / (k_2^{o'} c_o \alpha_3 \alpha \gamma F)$ as a function of the applied potential.

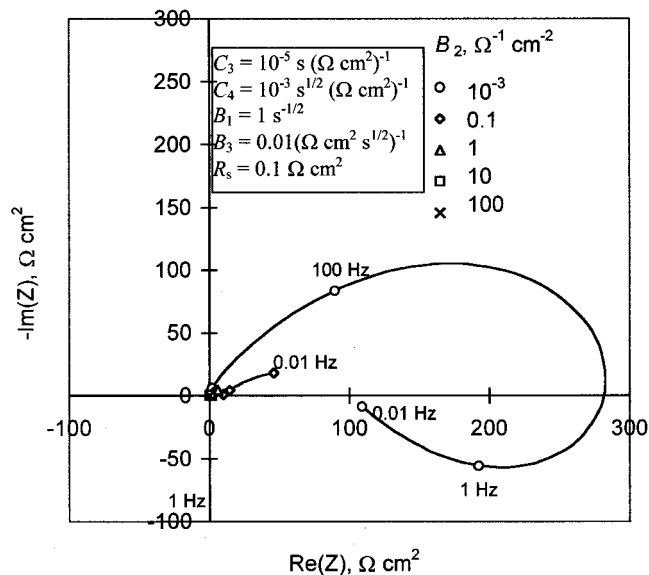
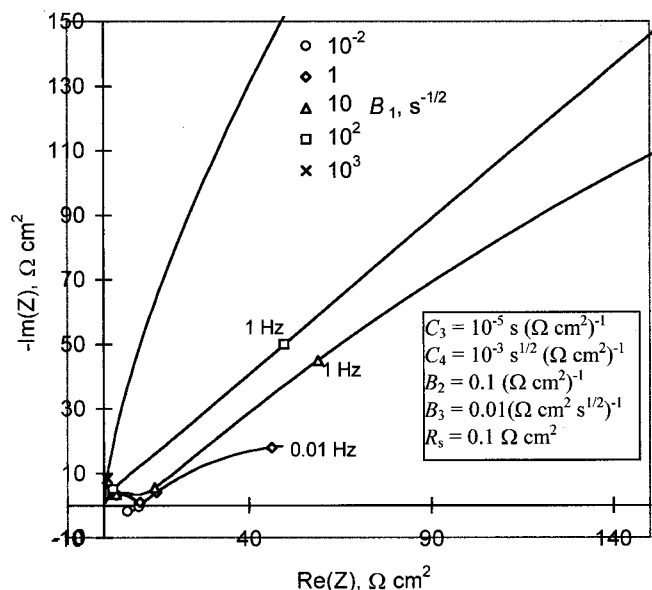
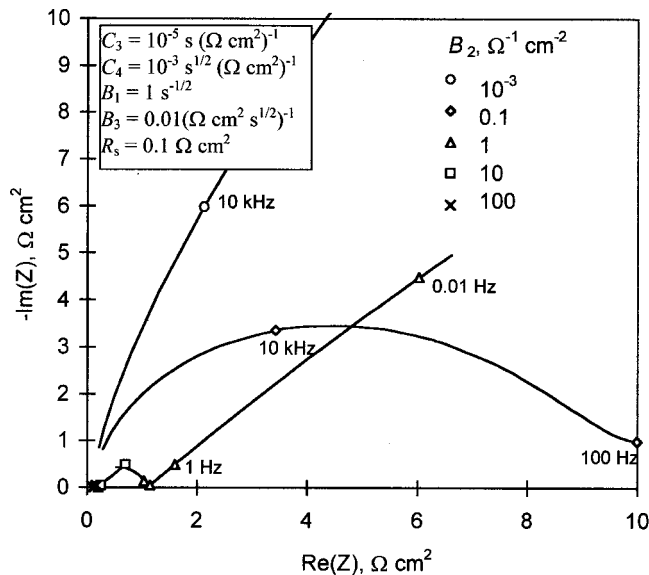
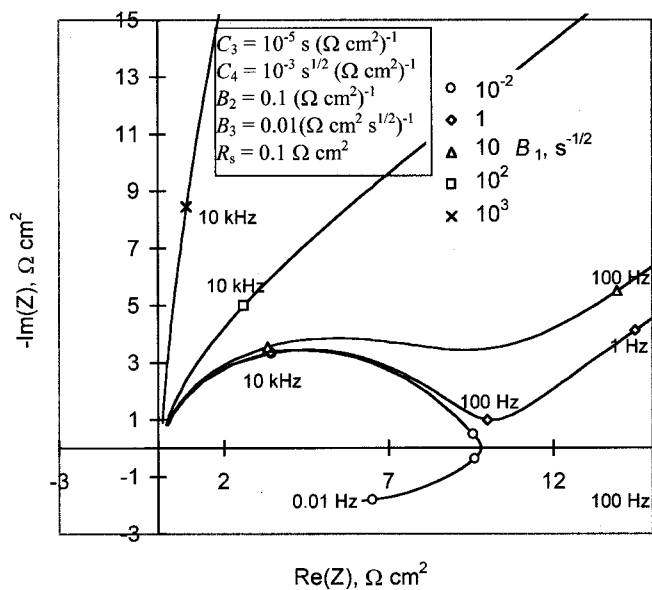


Figure 15. Nyquist plots for two different frequency ranges of the impedance function. B_2 is varied in the range 10^{-3} to 10^2 ($\Omega \text{ cm}^2$) $^{-1}$. Values of the remaining parameters are indicated in the box. Impedance data at four frequencies (0.01 Hz, 1 Hz, 100 Hz, and 10 kHz) are indicated for each case, but only few of these points have been labeled.

Figure 16. Nyquist plots for two different frequency ranges of the impedance function. B_2 is varied in the range 10^{-3} to 10^2 ($\Omega \text{ cm}^2$) $^{-1}$. Values of the remaining parameters are indicated in the box. Impedance data at four frequencies (0.01 Hz, 1 Hz, 100 Hz, and 10 kHz) are indicated for each case, but only few of these points have been labeled.

Two values of $k_3^{o'} e^{\alpha_3 \gamma (\beta \text{pH}_{\text{BOI}} + \phi_{\text{BOI}}^o + \alpha \phi_R)} \theta_o$ were derived via curve fitting as a function of the potential to 1 and 99 percent quantile data for $k_1^{o'} c_{\text{Li}}^{\text{MBI}} D_1 / (k_2^{o'} c_o \alpha_3 \gamma F)$, which were computed from 1 and 99 percent quantile data for D_1 in Tables I and II and Eq. 42. These two derived values define range limits for $k_3^{o'} e^{\alpha_3 \gamma (\beta \text{pH}_{\text{BOI}} + \phi_{\text{BOI}}^o + \alpha \phi_R)} \theta_o$, and are included in Table IV, term no. 1. From Eq. 27, data in Table III, bootstrap data for D_2 , and the extreme values for term no. 1 in Table IV, two sets of bootstrap data for $c_o \sqrt{0.5 D_W^{\text{SS}} / k_s^o}$ were calculated for each electrolyte system. The upper (lower) boundary of term no. 1 in Table IV was used to establish the lower (upper) boundary for $c_o \sqrt{0.5 D_W^{\text{SS}} / k_s^o}$ by computing the maximum (minimum) of its bootstrap data. These extreme values for $c_o \sqrt{0.5 D_W^{\text{SS}} / k_s^o}$ are listed in Table IV, term no. 2. From Eq. 20 and the two sets of bootstrap data for $c_o \sqrt{0.5 D_W^{\text{SS}} / k_s^o}$, two sets of

bootstrap data for $J_{\text{V} \infty} e^{-\alpha_3 \gamma (\beta \text{pH}_{\text{BOI}} + \phi_{\text{BOI}}^o + \alpha \phi_R)} / k_3^{o'}$, were calculated. The lower (upper) boundary for $J_{\text{V} \infty} e^{-\alpha_3 \gamma (\beta \text{pH}_{\text{BOI}} + \phi_{\text{BOI}}^o + \alpha \phi_R)} / k_3^{o'}$ (term no. 3 in Table IV) was selected as the minimum (maximum) of these bootstrap sets. The parameter ξ_1 in Table IV is defined as^{6,7}

$$\xi_1 = F \theta_o k_3^{o'} e^{-\alpha_3 \gamma (\beta \text{pH}_{\text{BOI}} + \phi_{\text{BOI}}^o + \alpha \phi_R)} \quad [46]$$

Values for ξ_1 , term no. 4 in Table IV, were reported (12 M KOH) or estimated (12 M KOH + 0.58 M sucrose) from data in Ref. 6. From these data and the range limits for term no. 1, boundary values for $(\alpha_3 + \alpha_h)(\beta \text{pH}_{\text{BOI}} + \phi_{\text{BOI}}^o + \alpha \phi_R)$ were derived and included in Table IV, term no. 5.

To facilitate interpretation of the results, it was assumed that $\alpha = 0.5$ (a reasonable selection; see for example, Ref. 25). Physical interpretation of the results are presented in Table V. Terms 2, 3, and 4 in Table V suggest faster water transport through the porous LiOH

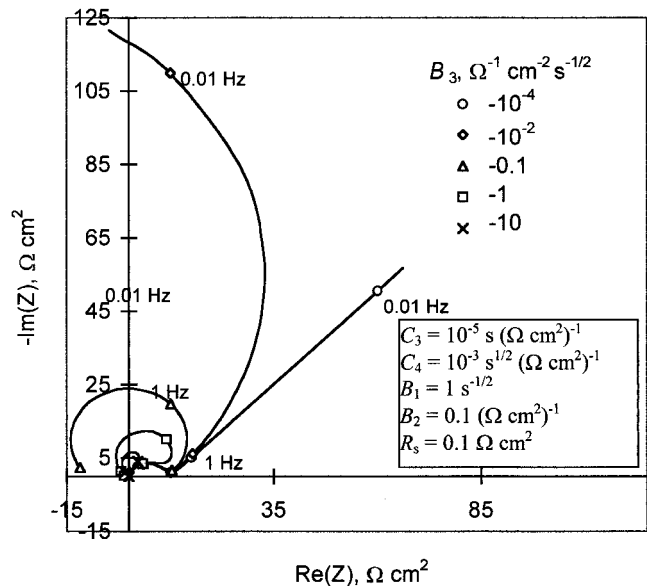
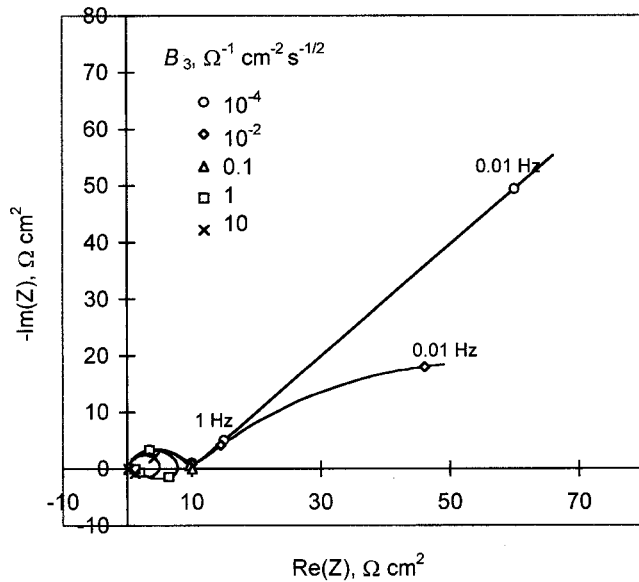
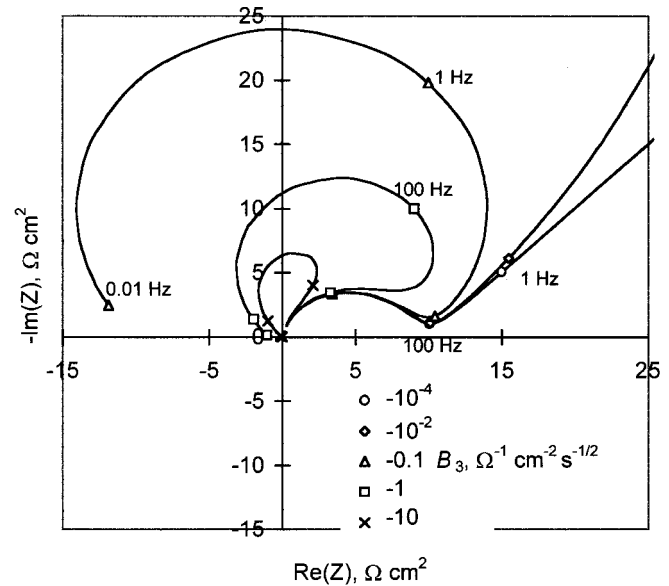
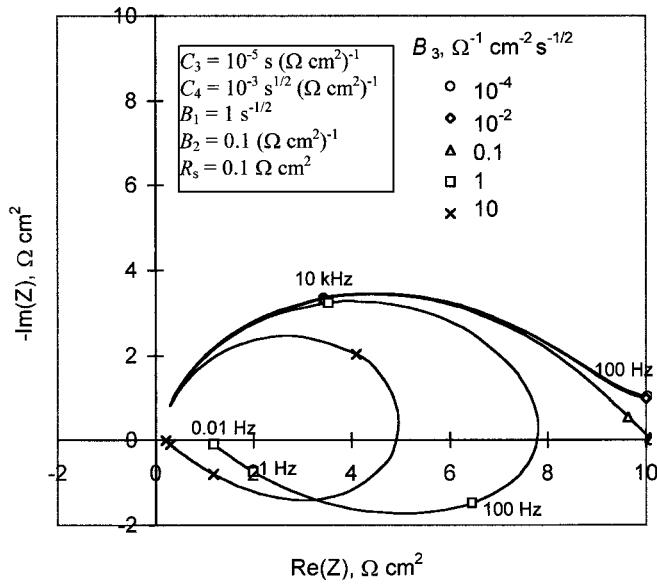


Figure 17. Nyquist plots for two different frequency ranges of the impedance function. B_3 is varied in the range 10^{-4} to $10 \Omega^{-1} \text{cm}^{-2} \text{s}^{-1/2}$. Values of the remaining parameters are indicated in the box. Impedance data at four frequencies (0.01 Hz, 1 Hz, 100 Hz, and 10 kHz) are indicated for each case, but only few of these points have been labeled.

Figure 18. Nyquist plots for two different frequency ranges of the impedance function. B_3 is varied in the range -10 to $-10^{-4} \Omega^{-1} \text{cm}^{-2} \text{s}^{-1/2}$. Values of the remaining parameters are indicated in the box. Impedance data at four frequencies (0.01 Hz, 1 Hz, 100 Hz, and 10 kHz) are indicated for each case, but only few of these points have been labeled.

outer layer, and higher standard rates of water consumption and LiH dissolution at the BOI for the 12 M KOH electrolyte system. Interestingly, terms 1 and 4 in table V suggest higher porosity, faster standard rates of water reduction, and injection of lithium cations into the solution for the 12 M KOH + 0.58 M sucrose electrolyte system. Furthermore, term no. 5 in Table IV indicates that the polarization of the BOI is also affected by the presence of sucrose. It must be noted that confidence intervals are not available for the steady-state parameters in Table III, and thus the ranges in Table V (partially derived from data in Table III) should be treated with caution. Note also that the wide confidence intervals for the 12 M KOH electrolyte system are the result of the small values of the steady-state faradaic admittance, dI_T^{ss}/dV , resulting in the small values for $|B_3|$ in Table I, and propagated throughout the computations.

The capacitance, C_3 , is comparable for both systems, and it may be argued that this is due to the similar geometric properties (e.g.,

thickness of the film in the two systems). On the other hand, C_4 is higher for the 12 M KOH electrolyte than for the 12 M KOH + 0.58 M sucrose electrolyte; i.e., the frequency dependence of the differential capacitance is more important in the 12 M KOH electrolyte system. This can be rationalized by noting that sucrose depresses the activity of the solution (i.e., lowers the rate of water transport through the outer layer and the rates of water consumption and LiH dissolution at the BOI). Therefore, the sucrose-free system is likely to respond faster to voltage perturbations, causing more noticeable dependencies of the geometric properties of the film on the voltage perturbation.

In the derivation of the impedance function, Eq. 1, steady-state constraints were invoked multiple times, as outlined throughout the paper. The impedance function was constructed by calibration to the zero frequency limit. Thus, it is expected that the low frequency impedance data would be well described by Eq. 1. At high frequen-

cies, the steady-state assumptions may break down. The functional form for the differential capacitance, Eq. 40, was also derived on the basis of steady-state constraints. However, the frequency range of validity of Eq. 1 and 40 cannot be decided *a priori*, and should be settled by comparison with experimental data. Note that in the high frequency range, from Eq. 29, $Z \rightarrow (i\omega C)^{-1} + R_s$. Thus, the differential capacitance, C (see Eq. 40), is the relevant component used to model the high frequency impedance loci, and the constant, R_s , is a term correcting limitations of the theory at high frequencies.

Equation 1 is compared to experimental data in Fig. 3-12. Best-fit parameters for the computation of the solid lines are displayed in boxes within the figures. Several impedance representations (Nyquist and Bode plots) were included for better appreciation of the goodness of fit. In the Bode plots for the phase, it is evident that the experimental and simulated impedance diverge at high frequencies, for some of the polarization potentials (e.g., Fig. 4, 5, 6, 7, 11, 12). Extrapolation of the experimental impedance to higher frequencies yields, in general, a solution resistance that is close to zero, a result that is consistent with the closeness of the Luggin probe to the lithium anode. Note the appreciable goodness of fit over most of the frequency range for some of the cases (e.g., Figures 3, 8, 9, 10). Equation 1 is valid for a wide frequency range and seems to break down only at frequencies above 3 kHz, for several cases.

It is of interest to present a collection of impedance signatures to identify other systems where Eq. 1 may be valid. Figures 13-18 display the variation of the Nyquist representation of the impedance as a function of the five parameters, B_1, B_2, B_3, C_3, C_4 , in Eq. 1. The impedance loci are drawn twice for two different frequency ranges to facilitate visualization of the high and low frequency regions. Some systems that have impedance signatures similar to those presented in Fig. 13-18 include beryllium,²⁶ ferri-ferrocyanide in KCl,²⁷ iron in H_2SO_4 ,^{28,29} iron in HNO_3 ,³⁰ and aluminum-lithium,³¹ to give just a few examples. Equation 1 was tested with impedance data in Ref. 32 (Ni-Cr alloys in sulfate solutions) with reasonable fits being achieved at high and low frequencies.

Figures 13 and 14 show the dependencies of the impedance function on C_3 and C_4 . If $C_4 \leq C_3$, the high frequency loci resembles a semicircle. Increasing the value of C_4 relative to that of C_3 causes the high frequency loci to decrease its curvature. When $C_4 \gg C_3$, the high frequency and low frequency "bumps" become undistinguishable (case $C_4 = 1 \text{ s}^{1/2} \Omega^{-1} \text{ cm}^{-2}$ in Fig. 14). From Eq. 1, the value of the impedance in the limit of zero frequency is B_1/B_3 . Thus, the impedance increases as B_1 increases (Fig. 15) or B_3 decreases (Fig. 17). Figure 16 indicates the obvious fact, from Eq. 1, that the magnitude of the impedance increases as $|B_2|$ increases. In Fig. 18, the low frequency impedance loci intersect the negative real axis, because the ratio B_1/B_3 is negative. In the limit of small B_3 , the plot resembles the electrochemical impedance of a process limited by diffusion (Warburg process), as shown by the case where $B_3 = 10^{-3} \Omega^{-1} \text{ cm}^{-2} \text{ s}^{-1/2}$ in Fig. 17, and by the case where $B_3 = -10^{-4} \Omega^{-1} \text{ cm}^{-2} \text{ s}^{-1/2}$ in Fig. 18. In principle, it is possible for C_3 and C_4 to be negative, providing more possibilities for the shape of the impedance locus that can be modeled by Eq. 1. The parameters used in generating Fig. 13-18 are known *a priori* to have physical significance, since they are comparable to the parameters in Tables I and II.

Conclusion

A model for the electrochemical impedance of lithium in alkaline (KOH) electrolytes has been developed. A technique for constructing an impedance function is presented that relies on calibration to steady-state properties. High frequency impedance data are explained on the basis of a differential capacitance that is voltage and frequency dependent, a property that has been rationalized theoretically. The impedance function is used to analyze the effect of an additive (e.g., sucrose) and KOH concentration on the properties of the lithium film. It is argued that sucrose decreases the rate of water transport through the outer LiOH layer, and also decreases the rates

of water consumption and LiH dissolution at the BOI. Sucrose seems to increase the porosity or enhance the standard rate of lithium-ion injection at the BOI, and also to change the BOI polarization. These results extend those discussed in Ref. 6, where it was argued that steady-state rates for lithium dissolution and hydrogen evolution, as functions of the electrolyte concentration, could be accounted for in terms of ξ_1 (see Eq. 46), without distinguishing effects on porosity, rate constants, or the BOI polarization. Shapes of several impedance signatures consistent with Eq. 1 are presented, and it is suggested that Eq. 1 may have wider applicability, and may be not just restricted to the lithium/water system.

Acknowledgments

The authors gratefully acknowledge the financial support of this work by the U.S. Government. The help by José R. Flores in generating the experimental data is appreciated.

The CNWRA assisted in meeting the publication costs of this article.

List of Symbols

a_j	activity of j species, dimensionless
A	surface area, m^2
A_1	see Eq. 20, $\text{s}^{1/2}$
B_1	see Eq. 30, $\text{s}^{-1/2}$
B_2	see Eq. 31, $\Omega^{-1} \text{ m}^{-2}$
B_3	see Eq. 32, $\Omega^{-1} \text{ m}^{-2} \text{ s}^{-1/2}$
B_W	see Eq. 13, V^{-1}
c_o	reference concentration, $c_o = 1 \text{ M}$
c_j	concentration of j species
C	effective specific film capacitance or differential capacitance, $\text{s} \Omega^{-1} \text{ m}^{-2}$
\hat{C}	specific film capacitance, $\text{s} \Omega^{-1} \text{ m}^{-2}$
C_o	specific film capacitance at V_o , $\text{s} \Omega^{-1} \text{ m}^{-2}$
C_3	see Eq. 40, $\text{s} \Omega^{-1} \text{ m}^{-2}$
C_4	see Eq. 40, $\text{s}^{1/2} \Omega^{-1} \text{ m}^{-2}$
D_1	see Eq. 26, $\Omega^{-1} \text{ m}^{-2}$
D_2	see Eq. 27, $\Omega^{-1} \text{ m}^{-2} \text{ s}^{1/2}$
D_W	diffusion coefficient of water through the outer layer, $\text{m}^2 \text{ s}^{-1}$
F	Faraday's constant, $F = 96485 \text{ C/mol}$
i	imaginary number, $i = \sqrt{-1}$
Im	imaginary part function
I_T	total current density, A/m^2
J_j	flux of j species, $\text{mol m}^{-2} \text{ s}^{-1}$
$J_{V\infty}$	see Eq. 18, $\text{mol m}^{-2} \text{ s}^{-1} \text{ V}^{-1}$
k_j	rate constant of reaction j, $\text{mol m}^{-2} \text{ s}^{-1}$
k_j^o	standard rate constant of reaction j, $\text{mol m}^{-2} \text{ s}^{-1}$
$k_j^o = k_j^o e^{-\alpha_j \eta_{BOI}^o}$	$\text{mol m}^{-2} \text{ s}^{-1}$
L_{bl}	barrier layer thickness, m
P	pore density per unit of outer layer cross section, m^{-2}
pH_{BOI}	pH at the barrier layer/outer layer interface
r_o	reference length, m
R	ideal gas constant, $R = 8.314 \text{ J mol}^{-1} \text{ K}^{-1}$
Re	real part function
R_s	constant, $\Omega \text{ m}^2$
sd	standard deviation
t	time variable, s
T	temperature, kelvin, $T = 298 \text{ K}$
V	time dependent applied potential, V
V_o	time independent applied potential, V
V_{bl}	potential drop, V
Y	admittance, $(\Omega \text{ m}^2)^{-1}$
Z	impedance, $\Omega \text{ m}^2$
Z_F	faradaic impedance, $\Omega \text{ m}^2$

Greek

α	polarizability of the barrier layer/outer layer interface, dimensionless
α_j	transfer coefficient of reaction j, dimensionless
β	proportionality constant, V
γ	$= F/RT$, V^{-1}
ΔX	perturbation in the X quantity
ΔV	$= \Delta V_o e^{i\omega t}$, harmonic potential perturbation, V
ΔV_o	amplitude of the harmonic potential perturbation, V
ε	electric field strength in the barrier layer, V m^{-1}
θ	outer layer porosity, dimensionless
$\theta_o = P \pi r_o^2$	dimensionless
κ_w	see Eq. 12, m^{-1}
μ	chemical potential, J mol^{-1}
ξ_1	see Ref. 6, A m^{-2}

ξ_2	constant, dimensionless
σ	surface charge density, C m ⁻²
ϕ	potential difference, V
ϕ_R	reference potential, V
ϕ_{BOI}^0	constant, V
ω	angular frequency, s ⁻¹

Subscript and Superscripts

BOI	quantity defined at the barrier layer/outer layer interface
LiOH	lithium hydroxide
Li ⁺	lithium cation
MBI	quantity defined at the metal/barrier layer interface
OH ⁻	hydroxide anion
V _H ⁻	hydrogen anion vacancy
V _{Li} ⁺	lithium cation vacancy
W, w	water
1, 2, 3, 4, s, h	quantity referred to Reactions 1-6 in Fig. 1
ss	steady state
O	reference constant or time-invariant quantity.
'	prime symbol, associated with kinetic parameters in Fig. 1

References

- O. Pensado-Rodríguez, M. Urquidi-Macdonald, and D. D. Macdonald, *J. Electrochem. Soc.*, **146**, 1318 (1999).
- D. D. Macdonald, *J. Electrochem. Soc.*, **139**, 3435 (1992).
- C. Y. Chao, L. F. Lin, and D. D. Macdonald, *J. Electrochem. Soc.*, **129**, 1874 (1982).
- L. F. Lin, C. Y. Chao, and D. D. Macdonald, *J. Electrochem. Soc.*, **128**, 1194 (1981).
- C. Y. Chao, L. F. Lin, and D. D. Macdonald, *J. Electrochem. Soc.*, **128**, 1187 (1981).
- O. Pensado-Rodríguez, J. R. Flores, M. Urquidi-Macdonald, and D. D. Macdonald, *J. Electrochem. Soc.*, **146**, 1326 (1999).
- O. Pensado-Rodríguez, M. Urquidi-Macdonald, J. R. Flores, and D. D. Macdonald, in *Passivity and Its Breakdown*, P. M. Natishan, H. S. Isaacs, M. Janik-Czachor, V. A. Macagno, P. Marcus, and M. Seo, Editors, PV 97-26, p. 870, The Electrochemical Society Proceedings Series, Pennington, NJ (1998).
- F. E. Pretzel, G. N. Rupert, C. L. Mader, E. K. Storms, G. V. Gritton, and C. C. Rushing, *J. Phys. Chem. Solids*, **16**, 10 (1960).
- T. A. Dellin, G. J. Dienes, C. R. Fischer, R. D. Hatcher, and W. D. Wilson, *Phys. Rev.*, **1**, 1745 (1970).
- P. A. Varotsos and S. Mourikis, *Phys. Rev. B*, **10**, 5220 (1974).
- M. Ikeya, *J. Phys. Soc. Jpn.*, **42**, 168 (1977).
- R. Pandey and A. M. Stoneham, *J. Phys. C*, **18**, 5289 (1985).
- E. Haque and A. K. M. A. Islam, *J. Phys. Chem. Solids*, **53**, 377 (1992).
- D. D. Macdonald and M. C. H. McKubre, in *Impedance Spectroscopy-Emphasizing Solid Materials and Systems*, J. R. Macdonald, Editor, Chap. 4, Wiley Interscience, New York (1987).
- M. E. Orazem, P. Agarwal, A. N. Jansen, P. T. Wojcik, and L. H. García-Rubio, *Electrochim. Acta*, **38**, 1903 (1993).
- R. D. Armstrong and K. Edmondson, *Electrochim. Acta*, **18**, 937 (1973).
- J. S. Newman, *Electrochemical Systems*, p. 39, 107-108, Prentice-Hall, Inc., Englewood Cliffs, NJ (1991).
- D. A. Frank-Kamenetskii, *Diffusion and Heat Transfer in Chemical Kinetics*, p. 107, Plenum Press, New York (1969).
- O. Pensado-Rodríguez, Ph.D. Thesis, Department of Engineering Science and Mechanics, The Pennsylvania State University, University Park, PA (1998).
- A. J. Bard and L. R. Faulkner, *Electrochemical Methods*, p. 500, John Wiley & Sons, New York (1980).
- J. R. Flores, Masters Thesis, Department of Engineering Science and Mechanics, The Pennsylvania State University, University Park, PA (1999).
- D. VanVoorhis, Ph.D. Thesis, Department of Engineering Science and Mechanics, The Pennsylvania State University, University Park, PA (1999).
- C. Gabrielli, *Identification of Electrochemical Processes by Frequency Response Analysis*, Solartron Instrumentation Group Monograph, The Solartron Electronic Groups Limited, Farnborough, England (1980).
- A. C. Cullen and H. C. Frey, *Probabilistic Techniques in Exposure Assessment: A Handbook for Dealing with Variability and Uncertainty in Models and Inputs*, p. 104, Plenum Press, New York (1999).
- D. D. Macdonald and M. Urquidi-Macdonald, *J. Electrochem. Soc.*, **137**, 2395 (1990).
- M. A. Hill, D. P. Butt, and R. S. Lillard, *J. Electrochem. Soc.*, **145**, 2799 (1998).
- C. Deslouis and B. Tribollet, *Electrochim. Acta*, **23**, 935 (1978).
- I. Epelboin, C. Gabrielli, M. Keddad, and H. Takenouti, *Comprehensive Treatise on Electrochemistry*, Vol. 4, J. O'M. Bockris, B. E. Conway, and E. B. Yeager, Editors, p. 151, Plenum Press, New York (1981).
- I. Epelboin, C. Gabrielli, M. Keddad, and H. Takenouti, *C. R. Seances Acad. Sci. Ser. 3*, **276**, 145 (1973).
- C. Gabrielli, M. Keddad, and H. Takenouti, *J. Electroanal. Chem.*, **61**, 367 (1975).
- I. Epelboin, M. Garreau, J. Thevenin, and D. Warin, *J. Electrochem. Soc.*, **127**, 2100 (1980).
- M. Bojinov, G. Fabricius, P. Kinnunen, T. Laitinen, K. Mäkelä, T. Saario, and G. Sundholm, *Electrochim. Acta*, **45**, 2791 (2000).